Atomic structure, electronic structure, and defect energetics in [001](310)Σ5 grain boundaries of $SrTiO_3$ and $BaTiO_3$

M. Imaeda,[1] T. Mizoguchi,[2,*] Y. Sato,[3] H.-S. Lee,[2] S. D. Findlay,[2] N. Shibata,[2] T. Yamamoto,[1,3] and Y. Ikuhara[2,3]
[1]*Department of Advanced Materials Science, The University of Tokyo, 5-1-5, Kashiwanoha, Kashiwa, Chiba 277-8561, Japan*
[2]*Institute of Engineering Innovation, The University of Tokyo, 2-11-16, Yayoi, Bunkyo, Tokyo 113-8656, Japan*
[3]*Nanostructures Research Laboratory, Japan Fine Ceramics Center, 2-4-1, Mutsuno, Atsuta-ku, Nagoya 456-8587, Japan*
(Received 15 July 2008; revised manuscript received 30 October 2008; published 24 December 2008)

In order to find relationships among the atomic structure, electronic structure, and defect energetics, [001](310)Σ5 grain boundaries (GBs) of $SrTiO_3$ and $BaTiO_3$ were investigated by using first-principles calculations and high-resolution scanning transmission electron microscopy. It was found that the rigid-body translations of one grain with respect to the other are indispensable to obtain the stable GB structure, and the rigid-body translation plays an important role to reduce the structural distortions such as dangling bonds and strains. It was clearly demonstrated that a fit of calculated structures with microscopy images is not enough to determine the GB structure unless O columns can be seen in the microscopy image. Although the vacancy formation energy depends on the atomic site, the defect energetics at the GB was found to be similar to that in the bulk. It was also found that Ti vacancy is more sensitive to the structural distortions than Sr(Ba) and O vacancies. This would be caused by the difference in the bonding character of Ti-O and Sr(Ba)-O. Through this study, the atomic structures of the [001](310)Σ5 GBs of $SrTiO_3$ and $BaTiO_3$ were determined, and the characteristic electronic structures and defect energetics of those GBs were identified.

DOI: 10.1103/PhysRevB.78.245320 PACS number(s): 68.35.Dv, 61.72.Mm

I. INTRODUCTION

$SrTiO_3$ and $BaTiO_3$ are typical perovskite oxides and are known to exhibit a large variety of electrical properties. Among their properties, nonlinear current-voltage (*I-V*) characteristics and positive temperature coefficient of resistivity (PTCR) arise in polycrystalline $SrTiO_3$ and $BaTiO_3$. Namely, grain boundaries (GBs) are indispensable to bring about those two properties. Due to their technological importance, the GBs of $SrTiO_3$ and $BaTiO_3$ have been extensively studied to understand and control the nonlinear *I-V* characteristics and PTCR properties.[1–4] From model experiments by using bicrystal, in which single GB with a certain orientation relationship and GB planes are present, it was found that the nonlinear *I-V* characteristics of $SrTiO_3$ and the PTCR of $BaTiO_3$ are dramatically changed by the GB characters such as crystallographic orientation, Σ value, and defect segregations.[3,5–8] This indicates that local atomic structures and nonstoichiometry of GB play important roles to determine such properties. In the vicinity of GBs, unusual strains and dangling bonds would be present and, thus, it is expected that defect energetics are different from those in bulk. Understanding those peculiar structures is required for further developments and applications of $SrTiO_3$ and $BaTiO_3$.

So far, several kinds of GBs of $SrTiO_3$, including [001](210)Σ5, [001](310)Σ5, Σ13, Σ17, [110](111)Σ3 twin, and random GBs, have been investigated by using atomic-resolution transmission electron microscopy (TEM) and scanning TEM (STEM), and local nonstoichiometry at the GBs were discussed by the combination with theoretical calculations.[9–27] Comparing with the studies for $SrTiO_3$ GB, although there are some reports on [110](111)Σ3 $BaTiO_3$ GB, the studies of the $BaTiO_3$ GB are limited;[28–32] that is, partially because $BaTiO_3$ single crystals are difficult to obtain.

Concerning the defect energetics, formation energy of point defects in $SrTiO_3$ and $BaTiO_3$ perfect crystals was systematically studied.[33–35] While special nonstoichiometric models, such as half occupancy, were also suggested in $SrTiO_3$ GB,[13,14,25,26] the energetics arguments have not been made to clarify the stability. In addition, defect formation energy at the individual sites of the GB and its relationships with the atomic structure and electronic structure of the GB have not been discussed in detail.

In this paper, first-principles calculations and high-resolution STEM observation were combined to reveal the atomic structure, electronic structure, and defect energetics of [001](310)Σ5 GBs of $SrTiO_3$ and $BaTiO_3$.

In order to determine the stable GB structures, rigid-body translations were considered in the present calculations. Although the importance of the rigid-body translation for obtaining the stable GB structure has been demonstrated,[27,36–38] some of the previous studies have not considered or have not mentioned the rigid-body translations.[13,14,25,26] After determining the stable structures of the GBs, the electronic structures and defect energetics in the vicinity of GBs were systematically investigated. The defect energetics of $SrTiO_3$ and $BaTiO_3$ were compared with each other and the difference between bulk and the GBs were discussed. Its aim was to find the relationships among the atomic structures, electronic structures, and defect energetics.

II. METHODOLOGY

A. Theoretical procedures for grain-boundary atomic structures

In this study, first-principles projector augmented wave (PAW) method within the generalized gradient approximation (GGA) implemented in VASP code was used.[39–41] Wave

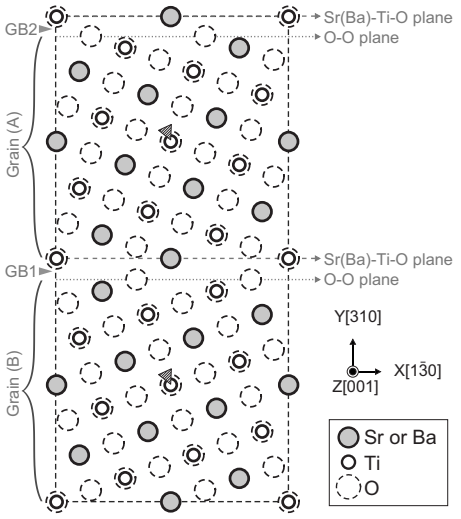

FIG. 1. An initial supercell consists of two equivalent GBs, GB1 and GB2. The GB has two termination planes Sr(Ba)-Ti-O plane and O-O plane. GB energies were calculated as a function of rigid-body translation of grain B with respect to grain A. The translations were considered in X, Y, and Z directions. Arrowed O atoms located in bulklike area were used to evaluate the rigid-body translation after optimization.

functions were expanded in a plane-wave basis set with a plane-wave cutoff energy of 330 eV. Before GB calculations, perfect crystalline $SrTiO_3$ (cubic) and $BaTiO_3$ (cubic) were calculated to optimize theoretical lattice constants. $BaTiO_3$ exhibits three types of polymorphs: monoclinic, tetragonal, and cubic. However, a cubic $BaTiO_3$ was assumed in this study to compare the results with those of $SrTiO_3$. In the calculation, the $10\times10\times10$ k-point mesh generated by the Monkhorst-Pack scheme (35 irreducible k points) was used for numerical integrations over the Brillouin zone. The optimized lattice constants in the present calculation were 3.942 Å for $SrTiO_3$ and 4.032 Å for $BaTiO_3$. They are in good agreement with previous studies.[33–35]

Next, supercells containing [001](310)Σ5 GBs were constructed. Figure 1 shows an example of the supercell including the two equivalent GBs. The GBs were made by rotating one grain by (A) 18.44° and the other grain by (B) −18.44° around [001] axis to construct Σ5 GB. In the GB supercell, three lattice vectors are represented as $X=[1\bar{3}0]$, $Y=[310]$, and $Z=[001]$ of the perovskite unit cell. Lengths of each vector of the supercell are $X=12.46$ Å, $Y=25.93$ Å, and $Z=3.942$ Å for $SrTiO_3$ and $X=12.75$ Å, $Y=26.50$ Å, and $Z=4.032$ Å for $BaTiO_3$. The total number of atoms in the supercell is 100. In the calculations, the $1\times1\times3$ k-point mesh generated by the Monkhorst-Pack scheme was used for numerical integrations over the Brillouin zone. As shown in Fig. 1, there are two different termination planes for the (310) surface in $SrTiO_3$ and $BaTiO_3$ with cubic perovskite crystal structure, Sr(Ba)-Ti-O plane, and O-O plane. In the present paper, we assumed that the GBs maintain charge neutrality. Therefore, O-O plane was chosen for one side and Sr(Ba)-Ti-O plane was for the other side as the termination planes because this is only a combination to keep the charge neutrality.

We took account of three-dimensional rigid-body translation (X, Y, and Z) of one grain with respect to the other. Figure 1 shows an initial structure with the translation state of $X=0$ Å, $Y=0.5$ Å, and $Z=0$ Å. Here, it was defined that (i) $Y=0$ Å when two termination planes at a GB are in the same position and (ii) $X=0$ Å and $Z=0$ Å when respective atoms [except for atoms on Sr(Ba)-Ti-O termination planes] in both grains have mirror symmetry with respect to the GBs. Increment of translation was 0.5 Å for all the dimensions. For each translation state, atomic structure in the supercell was optimized and GB energy was simultaneously calculated. During the atomic optimization, all atoms were allowed to move from their lattice sites, whereas the volume of the supercell was fixed.

After optimizing the GB atomic structure, strain and dangling bonds in the vicinity of the GB were evaluated. Dangling bonds were defined by the difference of numbers of coordinates between the GB supercell and perfect crystal. When interatomic distances from the surrounding atoms are shorter than a cutoff value, they were counted as coordinates. Here, the cutoff was defined to be 1.3 times of bond lengths in perfect crystals. Different cutoffs 1.1 and 1.2 times were also checked in the present paper, and it was confirmed that the tendency and arguments in this study did not change irrespective of the cutoff values. In order to evaluate the strains, the change in the bond length from perfect crystal was calculated and the ratio of the change was summed up by the number of bond. The obtained value was used as strain.

B. Theoretical procedures for defect formation energy

Based on the calculated structure of [001](310)Σ5 GBs, the supercell was expanded by duplicating three times in Z direction, and the supercell containing 300 atoms was used for the defect formation energy calculations. In the 300 atom supercells, the vacancy can be separated from the vacancies in the adjacent cells by more than 10 Å. To introduce a vacancy of Sr, Ba, Ti, and O, an atom was removed from the supercell. The vacancy formation energy at 27 sites [5 Sr(Ba) sites, 5 Ti sites, and 17 O sites] in the vicinity of GB was systematically calculated. In order to take account of atomic relaxations around a vacancy, selected atoms around the defect were relaxed. In the case of perfect crystalline $SrTiO_3$ and $BaTiO_3$ calculations, third nearest-neighbor atomic sites from the defect, which is approximately 4.2–4.3 Å apart from the defect, were allowed to relax.[33–35] On the other hand, it is difficult to define the exact third nearest neighbor in the GB models due to the structural complexity. Therefore, in the present GB models, atoms inside a sphere of 4.2–4.3 Å radius centered at the defect were relaxed until their residual forces were less than 0.1 eV/Å. Since large supercells containing 300 atoms were used, numerical integrations over the Brillouin zone were performed at the Γ point.

The formation energies of intrinsic defects in $SrTiO_3$ and $BaTiO_3$ were calculated by the same procedure as that in previous reports.[33,35,36] The formation energies of intrinsic defects depend on the chemical potentials of Sr, Ba, Ti, and

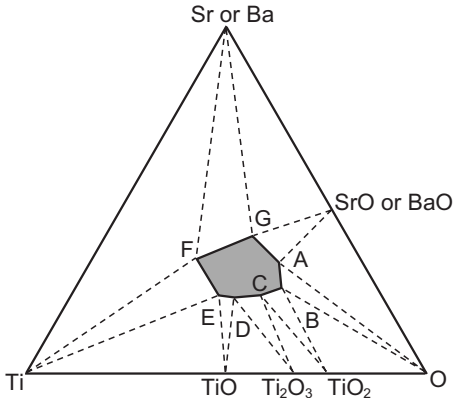

FIG. 2. Schematic phase diagram of the ternary system Sr(Ba)-Ti-O. A hatched polygon shows the region of $SrTiO_3$ ($BaTiO_3$). Corners of the polygon are indicated by $A-G$.

O and also vary with electronic chemical potential if a defect has a charge of q. For a defect with a charge q, its formation energy is given by

$$E_f = E_T(\text{defect}:q) - \{E_T(\text{GB}) - n_A\mu_A - n_B\mu_B - n_O\mu_O\} + q(\varepsilon_F + E_{\text{VBM}}). \quad (1)$$

Here, $E_T(\text{defect}:q)$ and $E_T(\text{GB})$ are the total energies of the GB supercell containing a defect in a charge state q and that of the GB supercell without any defect, respectively. n_A, n_B, and n_O are the numbers of Sr, Ba, Ti, and O atoms removed from the GB supercell to introduce a vacancy. μ_A, μ_B, and μ_O are the atomic chemical potentials and ε_F is the Fermi energy measured from the valence-band maximum (VBM). We considered charge-neutral (V^0_{Sr}, V^0_{Ba}, V^0_{Ti}, and V^0_{O}) and ionized (V^{2-}_{Sr}, V^{2-}_{Ba}, V^{2-}_{Ti}, V^{4-}_{Ti}, and V^{2+}_{O}) vacancies for possible atomic sites that will be shown later.

As can be seen Eq. (1), E_{VBM} needs to be determined. For this purpose, it was assumed that the electrostatic potentials in the GB supercell without vacancies were similar to those far from a defect in a GB supercell with a vacancy. This treatment can compensate distortion to the band structure around the band gap, which was caused by a vacancy.[42–46]

The Fermi level ε_F varied in the range of the band gap. The theoretical band gaps were found to be 1.78 eV of $SrTiO_3$ and 1.67 eV of $BaTiO_3$ by calculating the total energies of the charged perfect crystals, which are in good agreement with previous studies.[33–35,47–51] These values were smaller than the experimental values of 3.3 eV for both of $SrTiO_3$ and $BaTiO_3$. Differences (ΔE_g) between theoretical and experimental values are 1.52 eV for $SrTiO_3$ and 1.63 eV for $BaTiO_3$. As in previous investigations,[33,35,52] the formation energy of an O vacancy was corrected by adding a value of $m \times \Delta E_g$, where m was the number of electrons at the donor levels. For instance, the value of m equals 2 for V^0_O.

As mentioned above, the formation energies depend on the atomic chemical potentials. The chemical potentials of constituent atoms vary with equilibrium conditions among their related phases. Figure 2 shows a schematic phase diagram of the ternary Sr(Ba)-Ti-O system and the vertices of three phase regions were named $A-G$ as for the previous reports.[33,35] The values of atomic chemical potential of three elements were evaluated at those points. Here, it was assumed that $SrTiO_3$ and $BaTiO_3$ were always stable, so that the chemical potentials of the three elements were obtained from the combinations of the chemical potentials of Sr, SrO, Ba, BaO, Ti, TiO, Ti_2O_3, TiO_2, and O_2. The chemical potential of O_2 was obtained from the supercell calculation at the Γ point for an isolated O_2 molecule using a cubic supercell $15 \times 15 \times 15$ Å^3. Spin-polarized calculation was performed for the O_2. The errors in formation enthalpies for the rest of the materials due to spin-polarized and spin-unpolarized calculations might affect the vacancy formation energies. In order to check the errors, both of the spin-polarized and spin-unpolarized calculations were carried out. The heats of formation obtained from the calculations are summarized in Table I. It is seen that both spin-polarized and spin-unpolarized calculations satisfactorily reproduce the experimental values. Thus, in this study, the spin-unpolarized results were used for the atomic chemical potentials except for O_2.

TABLE I. Calculated and experimental formation enthalpies for the reference materials. The values in parentheses are calculated by the spin-polarized method. The experimental data were obtained from Ref. 53.

		Formation enthalpies (eV/atom)	
		Expt.	Calc.
BaO	*Fm3m*	−2.85	−2.96 (−2.99)
SrO	*Fm3m*	−3.07	−2.74 (−2.76)
TiO	*Fm3m*	−2.82	−2.47 (−2.48)
TiO_2	*P42/mmm*	−3.25	−3.13 (−3.12)
Ti_2O_3	*R3c*	−3.16	−3.04 (−3.06)

C. Experimental procedures

A $SrTiO_3$ bicrystal with [001](310)Σ5 GB was fabricated by joining two single crystals (Furuuchi Chem. Co. Ltd.) with the proper orientation. The procedure to fabricate the bicrystals has been reported in detail elsewhere.[5,6,54] A $BaTiO_3$ thin film was grown on the $SrTiO_3$ bicrystal by pulsed-laser deposition. The $BaTiO_3$ film was deposited at 750 °C substrate temperature in an O_2 atmosphere at a pressure of 1×10^{-3} Pa. A KrF excimer laser beam (wavelength of 248 nm; repetition frequency of 10 Hz) was used for the deposition.[55] TEM specimens of them were fabricated by a conventional method, including mechanical polishing, dimple gliding, and ion thinning. Those specimens were observed by aberration corrected STEM [JEOL JEM-2100F with a spherical aberration corrector (CEOS Gmbh)]. For high-angle annular dark-field (HAADF)-STEM observations, the probe-forming aperture was 23 mrad and the annular dark-field (ADF) detection range was from 81 to 221 mrad.

III. RESULTS AND DISCUSSION

A. Atomic structure of grain boundary

Figure 3 shows the theoretically calculated GB energies as a function of translation states. It is clearly seen that the

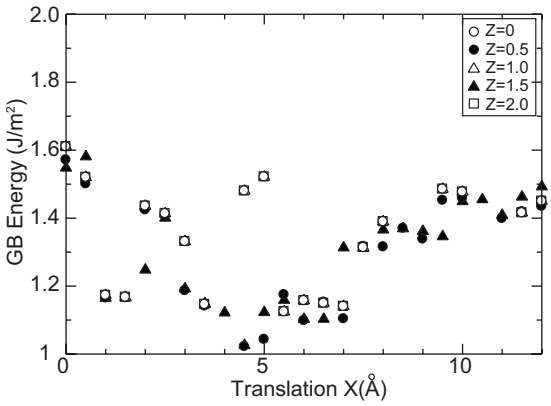

FIG. 3. GB energy of $SrTiO_3$ as a function of translation states. Data for $Y=0.5$ is shown.

GB energy changes with the translation, indicating the importance of rigid-body-translation consideration. The most stable GB energy was obtained by the translation state of $X=4.5$ Å, $Y=0.5$ Å, and $Z=0.5$ Å as the initial structure. Here, it should be mentioned that the translation state changed during the calculations due to the lattice relaxation and the translation state after the calculation was $X=4.4$ Å, $Y=0.5$ Å, and $Z=0.0$ Å. Namely, shifts of 0.1 and 0.5 Å to the X and Z directions took place. The GB energy of the most stable structure in this case was 1.02 J/m^2.

It is considered that this is an energetically stable structure and, thus, this structure is hereafter called "stable structure." The obtained structure is shown in Fig. 4(a). Some of previous studies on the $SrTiO_3$ GBs have not considered or have

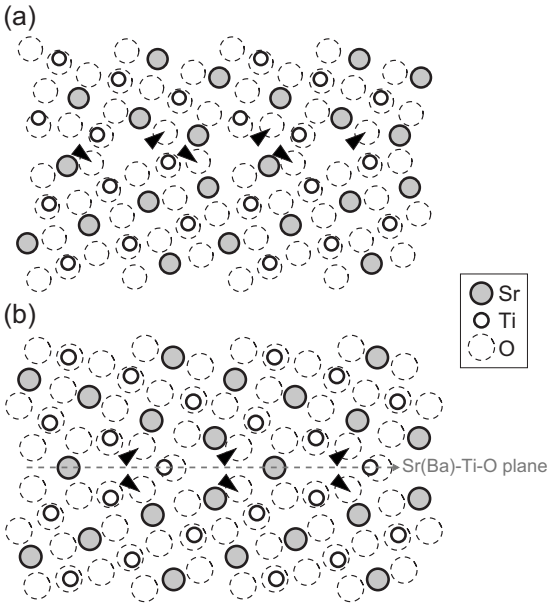

FIG. 4. (a) The stable $SrTiO_3$ GB structure obtained by using the initial translation state of $X=4.5$, $Y=0.5$, and $Z=0.5$. The translation state was changed to $X=4.4$, $Y=0.5$, and $Z=0$ during the structural optimization. (b) Mirror symmetric $SrTiO_3$ GB structure with the translation state of $X=0$, $Y=0.5$, and $Z=0$. Small and large solid circles and dotted circle represent Ti, Sr, and O, respectively. Arrows indicate certain O columns.

not mentioned such rigid body translation, and GB structures having mirror symmetry with respect to Sr-Ti-O plane have been mainly studied so far.[13,14,25,26] Such mirror symmetric structure was obtained by using the initial translation state of $X=0$ Å, $Y=0.5$ Å, and $Z=0$ Å [Fig. 4(b)]. It can be seen that not only cation sublattice but also anion sublattices are mirror symmetric with respect to the Sr-Ti-O plane. This calculated results, however, clearly revealed that such a "mirror symmetric" structure has a higher GB energy of 1.61 J/m^2 comparing to that in the most stable structure.

One of the reasons of the higher GB energy of the mirror symmetric structure can be found in the atomic structure of the GB. It is seen that the arrowed O atoms, they are located at almost the same position in Z direction, are close to each other (2.4 Å) in the mirror symmetric structure [Fig. 4(b)]. It is understood that such short-length O-O bonding is energetically unpreferable due to the electrostatic repulsion. On the other hand, in the stable structure, those O atoms are further away from each other [Fig. 4(a)]. Interestingly, their distance 2.8 Å corresponds to that in $SrTiO_3$ perfect crystal.

In order to confirm the validity of the calculated structure, experimental HAADF-STEM image was taken for the $[001](310)\Sigma5$ $SrTiO_3$ GB and the structure was compared with the calculated structures shown in Fig. 5. Since the image intensity of the HAADF-STEM image is approximately proportional to the square of atomic number (Z),[56] the brighter and darker columns correspond to Sr and Ti-O columns, respectively, whereas O column cannot be seen. It seems that the observed HAADF-STEM image is consistent with that observed in previous study.[10] In addition, it can be seen that the image intensity reduces at the GB core. At the present time, the origin of this reduction in the image intensity is not clarified; but it is expected that this is related to the structural distortions of the GB, thinner film thickness, or/and presence of the vacancy.

Here, both the stable structure [Fig. 5(c)] and the mirror symmetric structure [Fig. 5(d)] are compared with the experimental HAADF-STEM image [Fig. 5(b)]. In those figures, only cations were displayed to compare with the experimental image. Detailed inspections of the experimental image can find slight shift of one side of grain with respect to the other side of grain and such asymmetric structure is reproduced by the stable structure [Fig. 5(c)]. On the other hand, significant inconsistency with the experimental image is not found even in the mirror symmetric structure [Fig. 5(d)], though it does not reproduce the asymmetric structure. This is ascribed to the similarity of the cation sublattices between the stable structure and the mirror symmetric structure. As noted above, however, there is a significant difference in their O columns structure. The anion sublattice structures could not be identified by the present HAADF-STEM. This clearly indicates that a fit with HAADF-STEM image is not enough to determine the GB structure unless O columns can be seen.

Strains and dangling bonds in the stable GB structure are calculated and shown in Fig. 6. The dangling bonds are represented by the number and color tone [Fig. 6(a)], and the compressive and tensile strains are represented by red and blue colors, respectively [Figs. 6(b)]. It is seen that large structural distortions, namely, dangling bonds and large

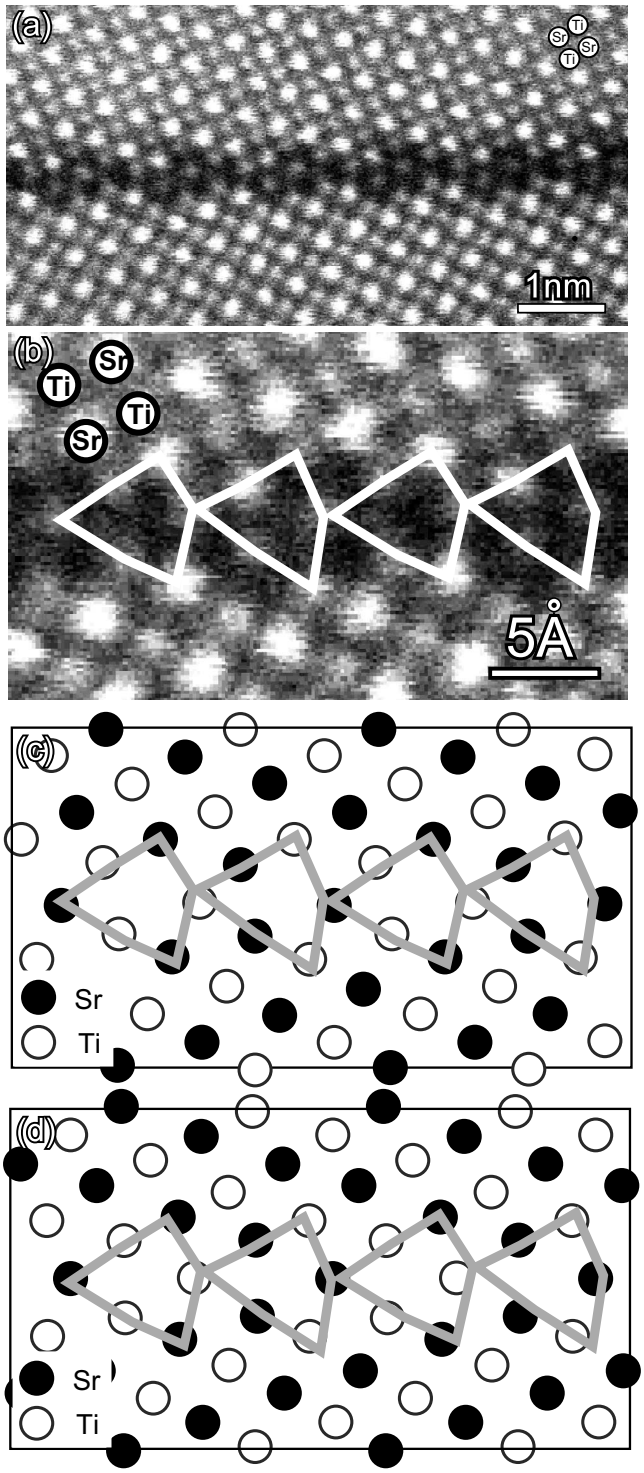

FIG. 5. (a) HAADF-STEM image of [001](310)Σ5 GB in a $SrTiO_3$ bicrystal. (b) Enlargement of the GB region. (c) Cation sublattice structure from the stable GB structure in Fig. 4(a), and (d) cation sublattice structure from the mirror symmetric GB structure in Fig. 4(b). Structural units of the boundary are indicated by polygons. Only cation sites are shown in the figures.

strains whose absolute values are larger than 2%, are mainly localized at the GB core and they distribute asymmetrically.

Here, the total number of the dangling bonds and the total strains in the supercell were evaluated. The total strains were

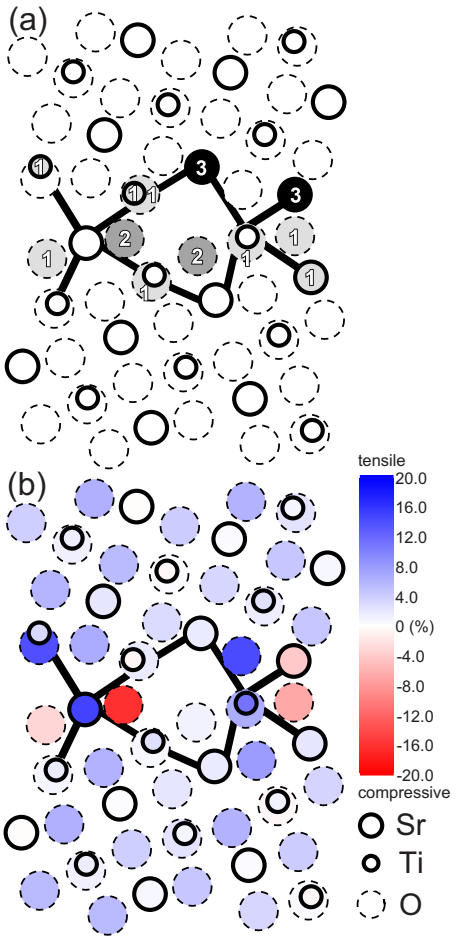

FIG. 6. (Color online) (a) The number of dangling bonds at each site of the stable $SrTiO_3$ GB structure. Open circles show the atomic sites without dangling bonds, whereas gray and black circles show the atomic sites with dangling bonds. Numbers in the circles denote the number of dangling bonds. (b) The magnitude of strain at each site of $SrTiO_3$ GB. The magnitude of compressive strain is indicated by red color and that of tensile strain is indicated by blue color. For both figures, structural units of the boundary are indicated by polygons.

obtained by summing up the absolute value of the strains. The total number of the dangling bonds and the total strains in the stable structure are estimated to be 16 and 296%, whereas that in the mirror symmetric structure is 16 and 321%, respectively. Namely, the rigid-body translation plays an important role to reduce the unpreferable distortions at the GB.

In the same manner as $SrTiO_3$, GB structure of [001](310)Σ5 $BaTiO_3$ was investigated. Figure 7 shows calculated GB energy as a function of the translation states. Several translation states (x=2.5–7.0 Å with z=0.0–1.0 Å) yielded similar final translation state of X=4.2, Y=0.5, and Z=0 and similar GB energies of 1.02 J/m^2, due to the relaxation. Detailed analyses revealed that the obtained structures are almost identical. During the calculations, atoms not only at GB but also in bulk regions are deviated and, as a result, several different initial translation states sank into the same final translation state. Similar behavior was also found in $SrTiO_3$ but the magnitude of deviation during the calcula-

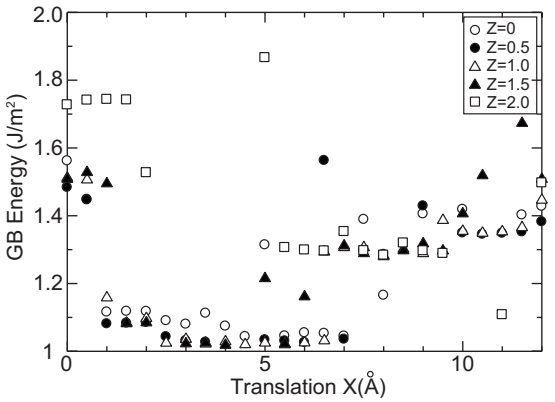

FIG. 7. Grain boundary energy of $BaTiO_3$ as a function of translation states. Data of $Y=0.5$ are shown.

tion is larger in $BaTiO_3$. This may indicate that $BaTiO_3$ is more sensitive to the structural distortions and is more likely to be the stable structure.

The stable GB structure is compared with the HAADF-STEM image in Fig. 8. It is seen that the calculated structure agrees well with the experimental image. The strains and dangling bonds are analyzed in Fig. 9. Ba and Ti at the GB core have strong tensile distortion, whereas both tensile and compressive distortions appear at the oxygen sites. Dangling bonds are mainly formed in the GB core. In addition to the atomic structure, it is found that the distribution of those structural distortions is very similar to that in $SrTiO_3$.

B. Electronic structure of grain boundary

To understand the GB electronic structure, partial density of states (PDOS) of selected atoms in the vicinity of GB was calculated. The selected Sr or Ba, Ti, and O are, respectively, numbered 1–5, 6–10, and 11–27, as shown in Figs. 10(a) and 10(b). PDOS of bulk region and GB region of the $SrTiO_3$ GB

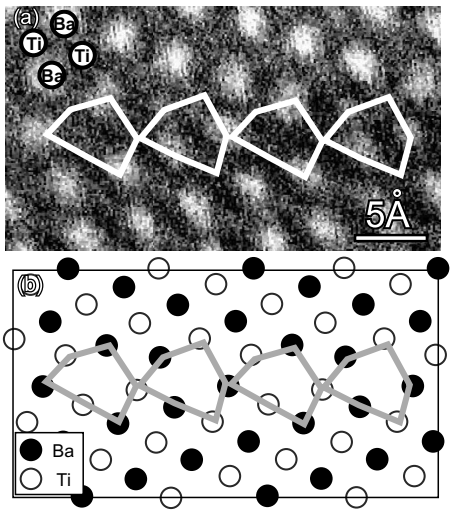

FIG. 8. (a) HAADF-STEM image of [001](310)Σ5 $BaTiO_3$ GB. (b) Cation sublattice structure from stable structure, which was obtained by calculation. Structural units of the boundary are indicated by polygons. Only cation sites are shown.

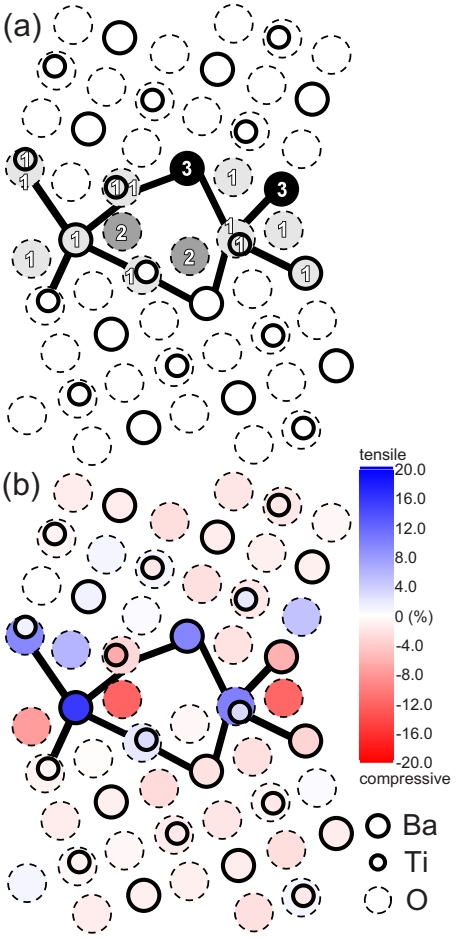

FIG. 9. (Color online) (a) The number of dangling bonds at each site of the stable $BaTiO_3$ GB structure. Open circles show the atomic sites without dangling bonds, whereas gray and black circles show the atomic sites with dangling bonds. Numbers in the circles denote the number of dangling bonds. (b) The magnitude of strain at each site of $BaTiO_3$ GB. The magnitude of compressive strain is indicated by red color and that of tensile strain is indicated by blue color. For both figures, structural units of the boundary are indicated by polygon.

supercell are shown in Figs. 11(a) and 11(b). The PDOS of the GB area was obtained by summing up the PDOS of those 27 sites and averaged them to fit to the stoichiometry, namely, Sr(Ba):Ti:O=1:1:3. The top of the valence band was aligned to zero. In PDOS from the bulk area, it can be seen that the strong O-Ti hybridization appears in the regions of −4.5–−2 eV, whereas the region of −2–0 eV is mainly composed of O. It is also found that Sr does not have strong hybridization with O in the occupied bands. In the unoccupied bands, it is found that Ti is dominant from 2 to 6 eV with a large peak around 4 eV. Although those characteristics also appear in the PDOS of GB area, overall profiles are broadened, which may originate from structural distortions at the GB. It should be mentioned that additional bands are not formed in the band gap even by the presence of the GB. In the case of $BaTiO_3$, it is found that overall characteristics are very similar to that of $SrTiO_3$ (Fig. 12). That is, strong O-Ti hybridizations are formed from −4.5 to −2 eV; Ti PDOS has

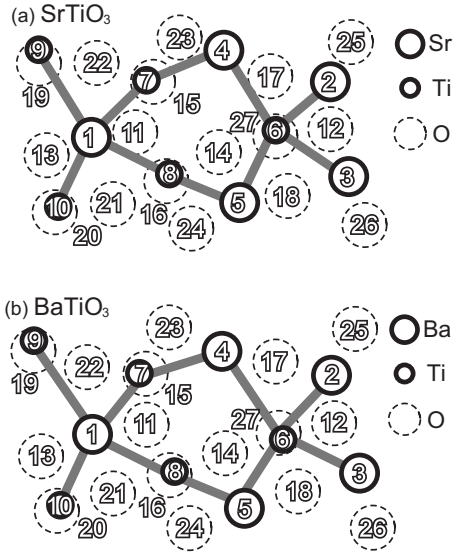

FIG. 10. (a) The stable GB structures of $SrTiO_3$ and (b) that of $BaTiO_3$. The sites in the vicinity of GB are numbered from 1 to 27. Structural units of the boundary are indicated by polygon.

strong peak around 4 eV and the PDOS of the GB area is more broadened than that of the bulk area.

Here, unoccupied Ti PDOS is focused because characteristic features were found. Figures 13 and 14 show PDOS from Ti sites in $SrTiO_3$ and $BaTiO_3$ GBs, respectively. Although the detailed profiles are different from each other, most of Ti sites have main peaks around 4 eV. However, it is found that the Ti9 sites in both $SrTiO_3$ and $BaTiO_3$ GBs have main peaks around 3 eV. Unoccupied Ti PDOS can be indirectly observed as Ti-$L_{2,3}$ edge of electron energy-loss spectra (EELS).[57] By using a modern aberration corrected STEM system, it is possible to obtain the spectrum nearly from a single atomic column.[58–60] Since the peaks of the Ti PDOS at

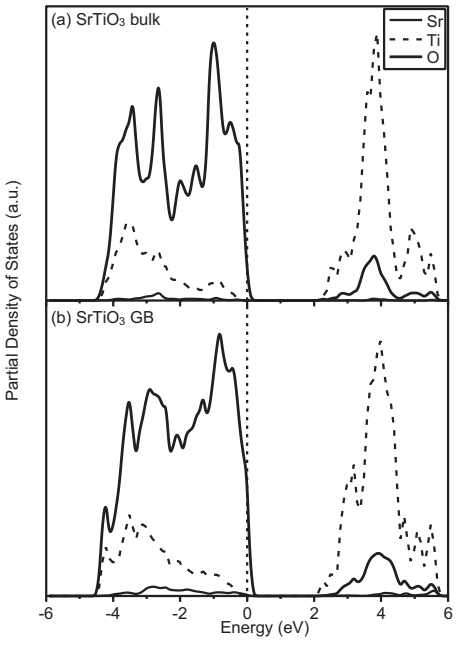

FIG. 11. Calculated PDOS of (a) bulk region and (b) GB region in the $SrTiO_3$ GB supercell. The PDOS of the GB area was obtained by summing up the PDOS of the 27 sites and averaged them to fit to the stoichiometry, namely, Sr:Ti:O=1:1:3. The top of the valence band was aligned to zero indicated by dashed line.

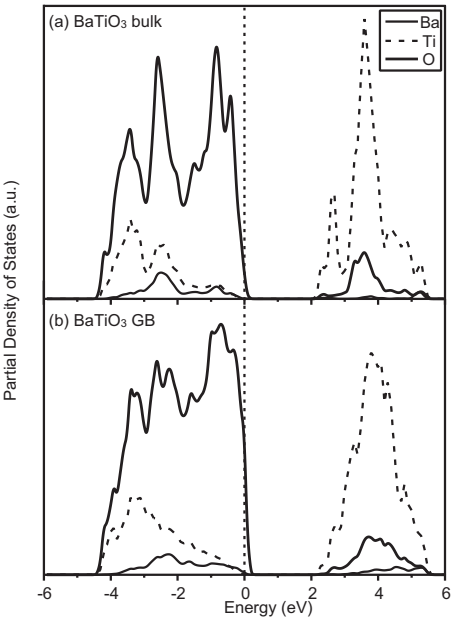

FIG. 12. Calculated PDOS of (a) bulk region and (b) GB region in the $BaTiO_3$ GB supercell. The PDOS of the GB area was obtained by summing up the PDOS of the 27 sites and averaged them to fit to the stoichiometry, namely, Ba:Ti:O=1:1:3. The top of the valence band was aligned to zero indicated by dashed line.

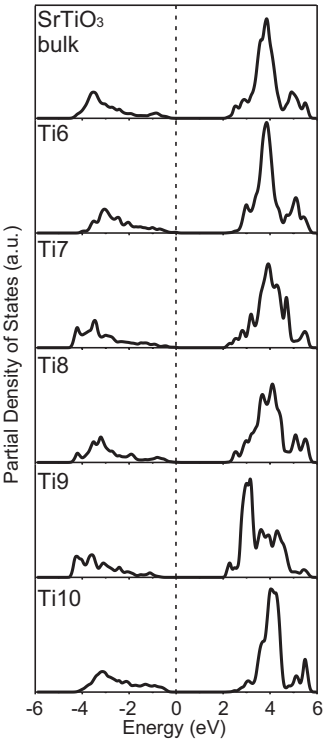

FIG. 13. Calculated Ti PDOS of bulk $SrTiO_3$ and each Ti site at $SrTiO_3$ GB. The top of the valence band was aligned to zero indicated by dashed line.

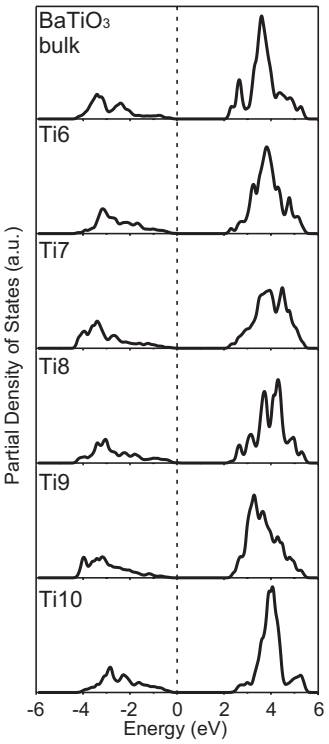

FIG. 14. Calculated Ti PDOS of bulk $BaTiO_3$ and each Ti site at $BaTiO_3$ GB. The top of the valence band was aligned to zero indicated by dashed line.

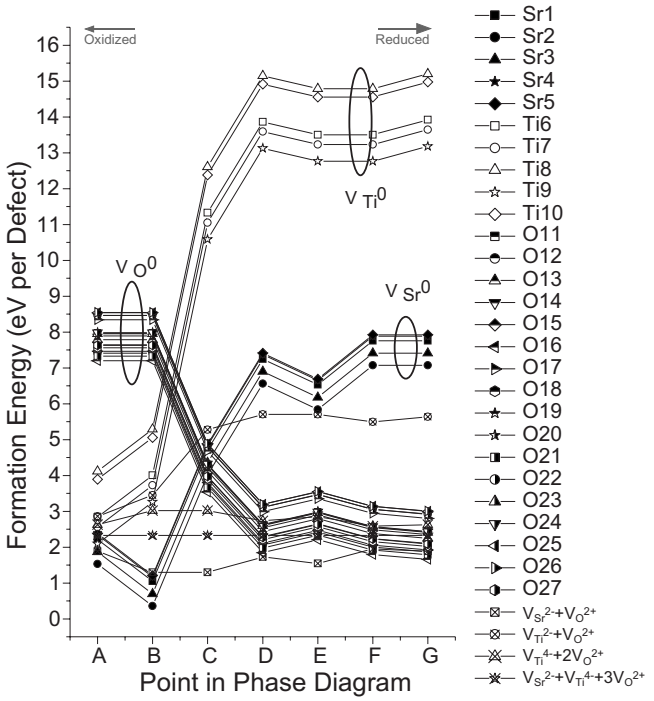

FIG. 15. Formation energy of a neutral vacancy at each atomic site of $SrTiO_3$ GB [Fig. 10(a)] at each equilibrium point (Fig. 2). Formation energies of Schottky defects are also shown. For Schottky defects, the lowest formation energy of respective species was selected and summed up according to the Schottky reactions.

3–4 eV are mainly composed of Ti 3*d* orbitals, changes in PDOS directly influence the spectral features of the Ti-$L_{2,3}$ edge. Especially, t_{2g} e_g splitting is expected to be sensitive to such structural distortions. This PDOS result predicts that the Ti-$L_{2,3}$ edge EELS changes mostly at Ti9 site. However, in order to discuss the spectral changes in detail, the first-principles multielectron calculation of the Ti-$L_{2,3}$ edge is required.[61–63]

C. Defect energetics of grain boundary

Based on the stable structures, vacancy formation energies of 27 sites in the vicinity of the GB (Fig. 10) were calculated. Dependence of vacancy formation energies at the atomic sites was considered using the results for neutral vacancies. On the other hand, Schottky reactions were considered using the results of ionized vacancies. From the results of vacancy formation energies for all the sites, the site with the lowest formation energy was selected for each species; in this study, Sr2, Ba2, Ti9, and O16 were used. Then, the formation energies were simply summed according to the Schottky formula. Schottky reactions considered here are as follows: $V_{Sr}^{2-}+V_O^{2+}$ (Sr partial Schottky), $V_{Ba}^{2-}+V_O^{2+}$ (Ba partial Schottky), $V_{Ti}^{2-}+V_O^{2+}$ (Ti partial Schottky), $V_{Ti}^{4-}+2V_O^{2+}$ (Ti partial Schottky), $V_{Sr}^{2-}+V_{Ti}^{4-}+3V_O^{2+}$ ($SrTiO_3$ full Schottky), and $V_{Ba}^{2-}+V_{Ti}^{4-}+3V_O^{2+}$ ($BaTiO_3$ full Schottky). Here, association between the vacancies was not considered. Since the following discussion focuses on neutral isolated vacancies and Schottky reactions, their formation energies will be independent of the Fermi energy. On the other hand, the formation energy is dependent on the atomic chemical potential as mentioned above.

In addition, the effect of the vacancy on the translation state should be mentioned. In order to check it, the rigid-body translation of ± 0.1 and ± 0.5 Å to X direction was again applied after making Sr2 vacancy in the stable structure. The calculated total energies at those translation states were found to be larger than that at the stable translation state. This may imply that the presence of the point defect does not change the stable translation state completely. However, it is expected that the effect should not be negligible when the vacancy concentration is large. This study focuses only on the isolated vacancy at the GB. Calculated formation energies at each point of the phase diagram shown in Fig. 2 are plotted in Figs. 15 and 16.

In both $SrTiO_3$ and $BaTiO_3$ cases, it is commonly seen that the formation energy changes with the atomic chemical potentials. There is a tendency that cation-related vacancies are more stable for more oxidized conditions, whereas O vacancies are more stable under more reduced conditions. In comparison with $SrTiO_3$ and $BaTiO_3$, formation energy of V_{Ti}^0 tends to be lower in $BaTiO_3$ than $SrTiO_3$, and the V_{Ti}^0 becomes the most stable species at point A in $BaTiO_3$. All these tendencies were similarly found in the perfect crystals of $SrTiO_3$ and $BaTiO_3$.[33,35]

In addition, formation energies also depended on the atomic sites at the GBs. Here, in order to find preferential defect formation site at the GB, the differences of defect formation energies between bulk region and GB, which is hereafter called ΔE_f, were calculated. ΔE_f in $SrTiO_3$ and

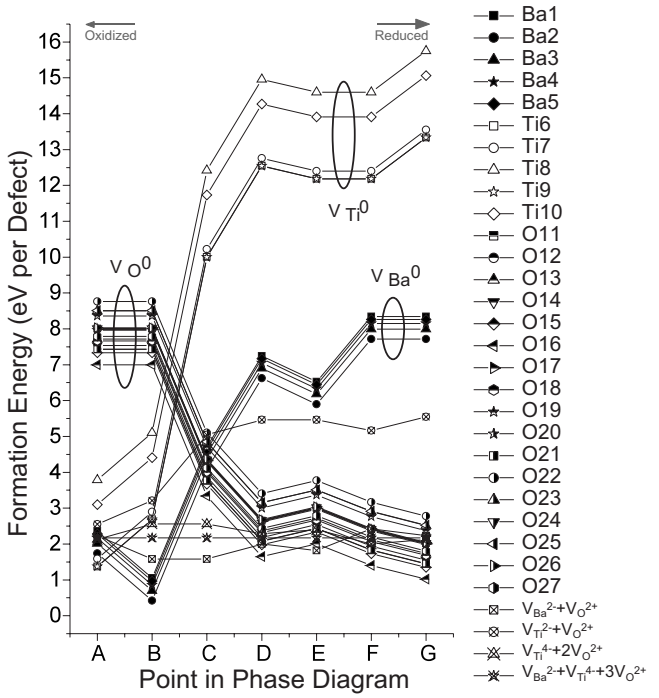

FIG. 16. Formation energy of a neutral vacancy at each atomic site of $BaTiO_3$ GB [Fig. 10(b)] at each equilibrium point (Fig. 2). Formation energies of Schottky defects are also shown. For Schottky defects, the lowest formation energy of respective species was selected and summed up according to the Schottky reactions.

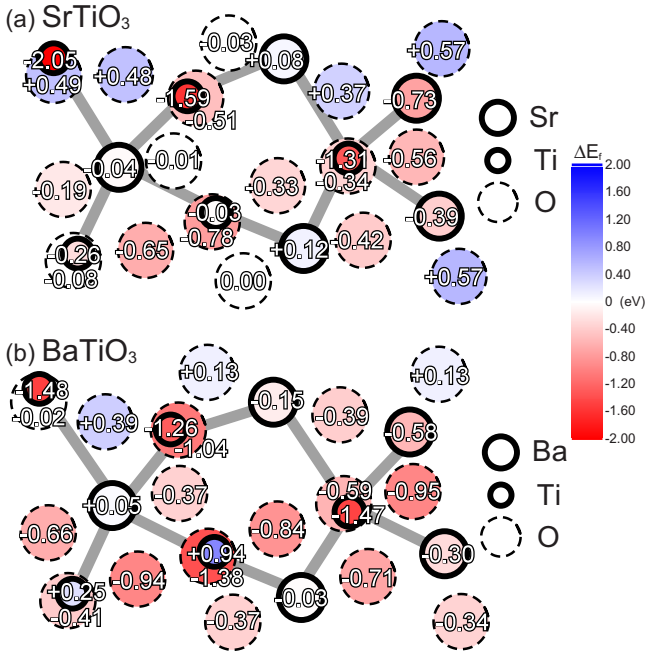

FIG. 17. (Color online) (a) The differences of defect formation energies (ΔE_f) between in bulk and at a certain GB atomic site in $SrTiO_3$ and (b) ΔE_f in $BaTiO_3$. The higher and lower defect energies than bulk are represented by blue and red colors, respectively. The numbers in the circles represent the value of ΔE_f.

$BaTiO_3$ GBs are shown in Fig. 17. The positive and negative ΔE_f are represented by blue and red colors. It can be seen that 19 sites for $SrTiO_3$ and 21 sites for $BaTiO_3$ have red colors, indicating that vacancies are more preferably formed at the GBs than that in bulk. It should be mentioned that Ti9 site, which has the smallest ΔE_f, corresponds with the site that has most different PDOS from bulk as discussed above (Figs. 13 and 14). In addition, it can be seen that the color distribution of Ti sites is apparently asymmetric. For instance, sites Ti9, Ti7, and Ti6 of both $SrTiO_3$ and $BaTiO_3$ have strong-red color, namely, much lower formation energy than that in bulk; whereas the sites in the other-side grain Ti10 and Ti8 have weak red or blue color. The asymmetric distribution of the ΔE_f for Ti vacancy may correspond to the asymmetric distributions of the strains and dangling bonds as shown in Figs. 6 and 9. On the other hand, such strong asymmetric distribution of the ΔE_f cannot be seen in Sr and Ba, even though strains and dangling bonds at those sites distribute asymmetrically. The origin of this difference will be discussed below.

D. Relationships among atomic structure, electronic structure, and defect energetics

In order to discuss the relationships among the structural distortions, electronic structure, and defect energetics, ΔE_f, number of dangling bonds, and strain at each atomic site are summarized in Tables II and III. The sites are sorted by ΔE_f, namely, top to bottom corresponds to smaller to larger ΔE_f. In addition to those structural distortions, the magnitude of relaxation due to the presence of vacancy was also evaluated by summing up total atomic motions occurred during the atomic relaxation. This is interesting comparison of ΔE_f and the magnitude of relaxation that the vacancy formation accompanying with larger relaxation tends to have lower formation energy, namely, smaller ΔE_f. In addition, it should be mentioned that the order of ΔE_f is similar in $SrTiO_3$ and $BaTiO_3$ though the absolute values are different. For instance, sites Ti9, O16, and Sr(Ba)2 commonly have the smallest ΔE_f in both $SrTiO_3$ and $BaTiO_3$ and sites Ti8, Ti10, O19, O22, O25, Sr(Ba)1, Sr(Ba)4, and Sr(Ba)5 have relatively large ΔE_f. In the case of [001](310)Σ5 GB, it can be concluded that the site dependence of the vacancy formation is very similar in $SrTiO_3$ and $BaTiO_3$ even though they are different materials.

Concerning the relationship between the defect energetics and the structural distortions, it seems that the formation energy of Ti vacancy is more related to the structural distortions than that of Sr(Ba) vacancy. For instance, the sites Ti9, Ti7, and Ti6, which have smaller ΔE_f, commonly have large strains and/or dangling bonds. On the other hand, although Sr(Ba)4 and Sr(Ba)1 have dangling bonds or large strains, their defect formation energy is close to bulk. Similarly, O11 and O19 sites have large strains and/or dangling bonds but the formation energies are similar to bulk. It is also found that the formation energy of Ti vacancy is more largely affected by the vacancy position than Sr(Ba) and O vacancies. The difference between the smallest and the highest ΔE_f for Ti vacancy is more than 2 eV; whereas that for the Sr(Ba) vacancy and O vacancy is less than 1 eV and approximately 1.5 eV, respectively. This implies that the Ti vacancy is more sensitive to the structural distortions than the Sr(Ba) and O vacancies.

TABLE II. The differences of formation energy (ΔE_f), the magnitude of relaxation, the number of dangling bonds, and the magnitude of strain in $SrTiO_3$ GB. The magnitude of relaxation (Å) was defined by the sum of changes of coordinates before and after relaxation. The sites are sorted by ΔE_f.

No.	ΔE_f(eV)	Magnitude of relaxation (Å)	No. of dangling bonds	Strain (%)
Sr2	−0.73	1.74	3	−4.10
Sr3	−0.39	1.85	1	1.85
Sr1	−0.04	1.88	0	14.6
Sr4	+0.08	1.71	2	1.54
Sr5	+0.12	1.71	0	1.56
Ti9	−2.05	3.33	1	2.88
Ti7	−1.59	3.04	1	−0.76
Ti6	−1.31	3.88	0	10.9
Ti10	−0.26	3.01	0	2.30
Ti8	−0.03	2.68	0	1.40
O16	−0.77	2.30	1	0.55
O21	−0.65	2.18	0	5.94
O12	−0.56	2.05	1	−6.64
O15	−0.51	3.23	1	1.50
O18	−0.41	2.42	0	7.76
O27	−0.34	2.38	0	6.21
O14	−0.33	2.00	2	0.99
O13	−0.19	2.04	1	−3.12
O20	−0.08	2.59	0	0.69
O23	−0.03	1.75	0	2.76
O11	−0.00	1.49	2	−16.1
O24	+0.00	2.23	0	1.85
O17	+0.37	1.48	0	14.1
O22	+0.48	1.16	0	6.43
O19	+0.49	1.20	0	13.6
O25	+0.57	1.17	0	4.28
O26	+0.57	1.17	0	3.28

TABLE III. The differences of formation energy (ΔE_f), the magnitude of relaxation, the number of dangling bonds, and the magnitude of strain in $BaTiO_3$ GB. The magnitude of relaxation (Å) was defined by the sum of change of coordinates before and after relaxation. The sites are sorted by ΔE_f.

No.	ΔE_f(eV)	Magnitude of relaxation (Å)	No. of dangling bonds	Strain (%)
Ba2	−0.58	1.69	3	−6.09
Ba3	−0.30	1.75	1	−3.37
Ba4	−0.15	1.74	2	9.50
Ba5	−0.03	1.56	0	−2.03
Ba1	+0.05	1.62	0	15.6
Ti9	−1.48	3.89	1	0.97
Ti6	−1.47	4.86	1	2.81
Ti7	−1.26	2.80	1	−6.43
Ti10	+0.25	2.94	0	−0.60
Ti8	+0.94	2.69	0	2.70
O16	−1.38	2.10	1	1.65
O15	−1.04	2.59	1	−2.89
O12	−0.95	1.92	1	−12.0
O21	−0.94	2.24	0	−0.09
O14	−0.84	2.80	2	−0.52
O18	−0.71	2.89	0	−2.39
O13	−0.66	1.83	1	−7.78
O27	−0.59	2.24	0	9.81
O20	−0.41	2.16	0	−0.89
O17	−0.39	1.43	1	−2.14
O11	−0.37	1.45	2	−12.0
O24	−0.37	1.80	0	−2.69
O26	−0.34	1.82	0	0.27
O19	−0.02	1.60	0	9.21
O23	+0.13	1.41	0	0.22
O25	+0.13	1.11	0	4.61
O22	+0.39	1.02	0	5.78

The different sensitivity can be attributed to the different bonding characters of Ti-O and Sr(Ba)-O. As discussed in Figs. 11 and 12, Ti has strong hybridization with O, whereas Sr or Ba does not have such strong hybridization. That is to say, Ti-O bonding and Sr(Ba)-O bonding are considered as covalent bonding and ionic bonding, respectively. Generally speaking, covalent bonding has strong directional character, whereas ionic bonding does not have it. Due to the directional and covalent Ti-O bondings, the formation energy of Ti vacancy is sensitive to the local-structure distortions; whereas the Sr or Ba vacancy is not so sensitive because Sr or Ba forms the nondirectional and ionic bondings with O.

IV. SUMMARY

By combining the first-principles calculation with the HAADF-STEM imaging, atomic structure, electronic structure, and defect energetics in [001](310)Σ5 grain boundaries of $SrTiO_3$ and $BaTiO_3$ were systematically investigated. The main results in this study are summarized as follows.

(1) By considering the rigid-body translations of one grain with respect to the other, the atomic structure of [001](310)Σ5 grain boundaries of $SrTiO_3$ and $BaTiO_3$ was determined. It was found that the rigid-body translation is indispensable to obtain the stable GB structure.

(2) Dangling bonds and large strains were mainly localized at the GB core and distribute asymmetrically. Detailed

analysis revealed that the rigid-body translation plays an important role to reduce those structural distortions.

(3) It was found that the experimental HAADF-STEM image was well reproduced by the stable GB structure. On the other hand, significant inconsistency with the experimental image was not found even in the mirror symmetric GB structure because it has similar cation sublattices structure to the stable GB structure. Their main difference, anion sublattice structures, could not be identified by the HAADF-STEM. This study demonstrated that a fit with HAADF-STEM image is not enough to determine the GB structure unless O columns can be seen in the image.

(4) It was found that characteristic electronic structures of bulk $SrTiO_3$ and $BaTiO_3$ are maintained in their GBs. However, detailed inspections of PDOS revealed that overall profiles of the PDOS are more broadened at the GBs than that in bulk. This PDOS analysis predicted that the Ti-$L_{2,3}$ edge EELS changes mostly at a specific Ti site in the GBs.

(5) Although the vacancy formation energy depends on the atomic site, it was found that cation-related vacancies are more stable at more oxidization conditions; whereas O vacancy is more preferable under more reduction conditions. In addition, the Ti-related vacancy can be the most stable species under oxidation condition in $BaTiO_3$, whereas the Sr-related vacancies are always more stable than Ti-related vacancies in $SrTiO_3$. Those characteristics were found to be similar to that in bulk.

(6) By calculating the difference of the vacancy formation energy between bulk and GBs (ΔE_f), it was found that most of atomic sites have negative ΔE_f, indicating that the vacancies preferentially form at the GB. It was also found that the Ti vacancy is more sensitive to the structural distortions than the Sr and O vacancies. This would be caused by the difference in the bonding characters of Ti-O and Sr-O.

Through this study, we determined the atomic structures of the $[001](310)\Sigma 5$ GBs of $SrTiO_3$ and $BaTiO_3$ and identified the characteristic electronic structures and defect energetics of the GBs. Even though they are different materials, we could find common characteristics both in $SrTiO_3$ and $BaTiO_3$. We successfully found some relationships among the atomic structure, electronic structure, and defect energetics.

Recent progresses of electron microscopy and first-principles method enable us to observe the GB with high resolution and calculate the GB within a realistic time, respectively. However, one should know that a fit of the calculated structure with TEM and STEM images is not enough to determine the atomic structure of GB because the O sites cannot be identified by usual TEM and STEM.

As we have shown here, GBs have different atomic structure, electronic structure, and defect energetic from bulk. The correct understanding of the atomic structure is indispensable to know those peculiar features of GBs. We believe that this manuscript demonstrated the way for the correct understanding of the GBs.

ACKNOWLEDGMENTS

We acknowledge R. Sakai for fabricating $BaTiO_3$ thin film and N. Saito for preparing TEM specimen. This study was partially supported by a Grant-in-Aid for Scientific Research in Priority Area "Nano Materials Science for Atomic Scale Modification 474," Young Scientists (B) 20760449, from the Ministry of Education, Sports, and Culture of Japan, and Izumi Science and Technology foundation (H18-J-06). One of the authors (Y.S.) is supported by the Japan Society for the Promotion of Science (JSPS).

*Corresponding author; Mizoguchi@sigma.t.u-tokyo.ac.jp

[1] M. Fujimoto and W. D. Kingery, J. Am. Ceram. Soc. **68**, 169 (1985).
[2] J. Gerblinger and H. Meixner, J. Appl. Phys. **67**, 7453 (1990).
[3] K. Hayashi, T. Yamamoto, and T. Sakuma, J. Am. Ceram. Soc. **79**, 1669 (1996).
[4] M. Kuwabara, K. Morimo, and T. Matsunaga, J. Am. Ceram. Soc. **79**, 997 (1996).
[5] M. Nishi, T. Tanaka, K. Matsunaga, Y. Ikuhara, and T. Yamamoto, Mater. Trans. **45**, 2112 (2004).
[6] T. Mizoguchi, Y. Sato, J. P. Buban, K. Matsunaga, T. Yamamoto, and Y. Ikuhara, Appl. Phys. Lett. **87**, 241920 (2005).
[7] T. Yamamoto, Y. Sato, T. Tanaka, K. Hayashi, Y. Ikuhara, and T. Sakuma, J. Mater. Sci. **40**, 881 (2005).
[8] T. Yamamoto and Y. Ikuhara, J. Electron Microsc. **50**, 485 (2001).
[9] M. M. McGibbon, N. D. Browning, M. F. Chisholm, A. J. McGibbon, S. J. Pennycook, V. Ravikumar, and V. P. Dravid, Science **266**, 102 (1994).
[10] N. D. Browning and S. J. Pennycook, J. Phys. D. **29**, 1779 (1996).
[11] N. D. Browning, S. J. Pennycook, M. F. Chisholm, M. M. McGibbon, and A. J. McGibbon, Interface Sci. **2**, 397 (1995).
[12] M. M. McGibbon, N. D. Browning, A. J. McGibbon, and S. J. Pennycook, Philos. Mag. A **73**, 625 (1996).
[13] M. Kim, G. Duscher, N. D. Browning, K. Sohlberg, S. T. Pantelides, and S. J. Pennycook, Phys. Rev. Lett. **86**, 4056 (2001).
[14] V. Ravikumar, V. P. Dravid, and D. Wolf, Interface Sci. **8**, 157 (2000).
[15] V. P. Dravid and V. Ravikumar, Interface Sci. **8**, 177 (2000).
[16] V. Ravikumar and V. P. Dravid, Ultramicroscopy **52**, 557 (1993).
[17] N. D. Browning, J. P. Buban, H. O. Moltaji, S. J. Pennycook, G. Duscher, K. D. Johnson, R. P. Rodrigues, and V. P. Dravid, Appl. Phys. Lett. **74**, 2638 (1999).
[18] H. O. Moltaji, J. P. Buban, J. A. Zaborac, and N. D. Browning, Micron **31**, 381 (2000).
[19] Z. Zhang, W. Sigle, F. Phillipp, and M. Rühle, Science **302**, 846 (2003).
[20] O. Kienzle and F. Ernst, J. Am. Ceram. Soc. **80**, 1639 (1996).
[21] O. Kienzle, M. Exner, and F. Ernst, Phys. Status Solidi A **166**, 57 (1998).
[22] S. Hutt, S. Köstlmeier, and C. Elsässer, J. Phys.: Condens. Mat-

ter **13**, 3949 (2001).
[23] N. D. Browning, H. O. Moltaji, and J. P. Buban, Phys. Rev. B **58**, 8289 (1998).
[24] R. F. Klie and N. D. Browning, Appl. Phys. Lett. **77**, 3737 (2000).
[25] S-D. Mo, W. Y. Ching, M. F. Chisholm, and G. Duscher, Phys. Rev. B **60**, 2416 (1999).
[26] H. Chang, Y. Choi, J. D. Lee, and H. Yi, Appl. Phys. Lett. **81**, 3564 (2002).
[27] R. Astala and P. D. Bristowe, J. Phys.: Condens. Matter **14**, 13635 (2002).
[28] C. L. Jia, K. Urban, M. Mertin, S. Hoffmann, and R. Waser, Philos. Mag. A **77**, 923 (1998).
[29] C. L. Jia and A. Thust, Phys. Rev. Lett. **82**, 5052 (1999).
[30] W. T. Geng, Y. J. Zhao, A. J. Freeman, and B. Delley, Phys. Rev. B **63**, 060101(R) (2000).
[31] C. L. Jia, Philos. Mag. Lett. **79**, 99 (1999).
[32] C. L. Jia and K. Urban, Science **303**, 2001 (2004).
[33] T. Tanaka, K. Matsunaga, Y. Ikuhara, and T. Yamamoto, Phys. Rev. B **68**, 205213 (2003).
[34] H. Moriwake, Int. J. Quantum Chem. **99**, 824 (2004).
[35] H. Lee, T. Mizoguchi, T. Yamamoto, S. Kang, and Y. Ikuhara, Act. Mater. **55**, 6535 (2007).
[36] H. Nishimura, K. Matsunaga, T. Saito, T. Yamamoto, and Y. Ikuhara, J. Am. Ceram. Soc. **86**, 574 (2003).
[37] F. Oba, I. Tanaka, S. R. Nishitani, H. Adachi, B. Slater, and D. H. Gay, Philos. Mag. A **80**, 1567 (2000).
[38] Y. Sato, T. Mizoguchi, F. Oba, Y. Ikuhara, and T. Yamamoto, Phys. Rev. B **72**, 064109 (2005).
[39] G. Kresse, Ph.D. thesis, Technische Universität, 1993.
[40] G. Kresse and J. Furthmüller, Comput. Mater. Sci. **6**, 15 (1996).
[41] J. P. Perdew, J. A. Chevary, H. Vosko, K. A. Jackson, M. R. Pederson, D. J. Singh, and C. Fiolhais, Phys. Rev. B **46**, 6671 (1992).
[42] K. Matsunaga, T. Tanaka, T. Yamamoto, and Y. Ikuhara, Phys. Rev. B **68**, 085110 (2003).
[43] D. B. Laks, C. G. Van de Walle, G. F. Neumark, P. E. Blöchl, and S. T. Pantelides, Phys. Rev. B **45**, 10965 (1992).
[44] A. García and J. E. Northrup, Phys. Rev. Lett. **74**, 1131 (1995).
[45] S. Pöykkö, M. J. Puska, and R. M. Nieminen, Phys. Rev. B **53**, 3813 (1996).
[46] T. Mattila and A. Zunger, Phys. Rev. B **58**, 1367 (1998).
[47] S. Kimura, J. Yamauchi, M. Tsukada, and S. Watanabe, Phys. Rev. B **51**, 11049 (1995).
[48] E. Heifets, R. I. Eglitis, E. A. Kotomin, J. Maier, and G. Borstel, Phys. Rev. B **64**, 235417 (2001).
[49] J. Padilla and D. Vanderbilt, Phys Rev B **56**, 1625 (1997).
[50] X. Y. Xue, C. L. Wang, and W. L. Zhong, Surf. Sci. **550**, 73 (2004).
[51] R. Khenata, M. Sahnoun, H. Baltache, M. Rérat, A. H. Rashek, N. Illes, B. Bouhafs, Solid State Commun. **136**, 120 (2005).
[52] S. B. Zhang and J. E. Northrup, Phys. Rev. Lett. **67**, 2339 (1991).
[53] W. G. Mallard, P. J. Linstrom, *NIST Chemistry Webbook*, NIST Standard Reference Database No. 69 (National Institute of Standards and Technology, Gaithersburg, MD, 2003).
[54] S. Y. Choi, J. P. Buban, M. Nishi, H. Kageyama, N. Shibata, T. Yamamoto, S. J. Kang and Y. Ikuhara, J. Mater. Sci. **41**, 2621 (2006).
[55] M. Igarashi, Y. Sato, N. Shibata, T. Yamamoto, and Y. Ikuhara, J. Mater. Sci. **41**, 5146 (2006).
[56] S. J. Pennycook and D. E. Jesson, Phys. Rev. Lett. **64**, 938 (1990).
[57] R. F. Egerton, *Electron Energy-loss Spectroscopy in the Electron Microscope* (Plenum, New York, 1996).
[58] M. Varela, S. D. Findlay, A. R. Lupini, H. M. Christen, A. Y. Borisevich, N. Dellby, O. L. Krivanek, P. D. Nellist, M. P. Oxley, L. J. Allen, and S. J. Pennycook, Phys. Rev. Lett. **92**, 095502 (2004).
[59] H. Ohta, S. W. Kim, Y. Mune, T. Mizoguchi, K. Nomura, S. Ohta, T. Nomura, Y. Nakanishi, Y. Ikuhara, M. Hirano, H. Hosono, and K. Koumoto, Nature Mater. **6**, 129 (2007).
[60] T. Mizoguchi, M. Varela, J. P. Buban, T. Yamamoto, and Y. Ikuhara, Phys. Rev. B **77**, 024504 (2008).
[61] K. Ogasawara, T. Iwata, Y. Koyama, T. Ishii, I. Tanaka and H. Adachi, Phys. Rev. B **64**, 115413 (2001).
[62] H. Ikeno, T. Mizoguchi, Y. Koyama, Y. Kumagai, and I. Tanaka, Ultramicroscopy **106**, 970 (2006).
[63] H. Ikeno, I. Tanaka, Y. Koyama, T. Mizoguchi, and K. Ogasawara, Phys. Rev. B **72**, 075123 (2005).